Journal of Computational Physics 228 (2009) 2082–2091

Contents lists available at ScienceDirect

Journal of Computational Physics

journal homepage: www.elsevier.com/locate/jcp

A constant-density approach for incompressible multi-phase SPH

X.Y. Hu *, N.A. Adams

Lehrstuhl für Aerodynamik, Technische Universität München, Boltzmannstr. 15, 85748 Garching, Germany

ARTICLE INFO

Article history:
Received 8 May 2008
Received in revised form 14 October 2008
Accepted 24 November 2008
Available online 9 December 2008

Keywords:
Multi-phase flows
Incompressible flow
Particle method

ABSTRACT

A constant-density approach, which corrects intermediate density errors by adjusting the half-time-step velocity with exact projection, is proposed for the multi-phase SPH method developed in our previous work [X.Y. Hu, N.A. Adams, An incompressible multi-phase SPH method, J. Comput. Phys. 227 (2007) 264–278]. As no prescribed reference pressure is required, the present approach introduces smaller numerical viscosity and allows to simulate flows with unprecedentedly high density ratios by the projection SPH method. Numerical examples for Taylor–Green flow, capillary waves and for Rayleigh–Taylor instability are presented and compared to theoretical solutions or references from the literature.

1. Introduction

In our previous work [7], an incompressible multi-phase SPH method is proposed for flows with sharp density and viscosity interfaces. To handle the problem of accumulating density errors and particle clustering, which can occur with the projection SPH method [2,12,11], a constant-density constraint has been proposed by correcting the particle position with an iterative approach. While numerical examples demonstrate that this approach is more accurate and more efficient than previous SPH for flow with low density ratios, it faces similar difficulties when the density ratio is high. First, the convergence behavior of the iterative scheme is difficult to estimate *a priori* due to the non-linear relation between particle position and particle density. When the density ratio is high, the iteration may fail to converge to the permitted maximum density error. Second, a prescribed reference pressure, which is superimposed onto the pressure distribution for the constant-density and the zero-velocity-divergence constraints, is required to avoid the tensile instability [13,3]. Although good accuracy can be obtained with an optimal reference pressure from numerical experimentation, extra numerical viscosity may be introduced if the reference pressure is over-estimated. In addition, there is a time-step criterion based on the prescribed reference pressure. Since the reference pressure is proportional to the maximum density, it can lead to extremely small time-step sizes for problems with high density ratios.

In this paper, the constant-density constraint is imposed by a new technique allowing to simulate flows with high density ratios of 100 or more, which has not been achieved by previous projection SPH methods. Other than the non-linear iterative correction of the particle position in Ref. [7], the present method modifies the half-time-step velocity by an one-step correction based on an exact projection approach. Since only a linear system is involved, the convergence behavior of the iterative scheme can be estimated *a priori*. With exact projection, no reference pressure is required to be superimposed for the constant-density constraint step, and the reference pressure for the zero-velocity-divergence constraint can be treated in a simple way. Therefore, the extra numerical viscosity due to an over-estimated reference pressure in Ref. [7] can be avoided. Unlike the previous time-step criterion based on the reference pressure in Ref. [7], a criterion based on the predicted density

* Corresponding author. Tel.: +49 89 28916152; fax: +49 89 289 16139.
E-mail address: xiangyu.hu@aer.mw.tum.de (X.Y. Hu).

0021-9991/$ - see front matter © 2008 Elsevier Inc. All rights reserved.
doi:10.1016/j.jcp.2008.11.027

error and the accumulated density error during previous steps is formulated. Since it is not directly related to the reference pressure or the density ratio, the related obstacle of small time-step sizes is alleviated. To evaluate the performance of the present method, numerical tests are carried out and compared to analytical and previous results.

2. Method

As in Ref. [7], we consider the incompressible, multi-phase and isothermal Navier–Stokes equations in a Lagrangian frame

$$\frac{d\rho}{dt} = 0 \quad \text{or } \nabla\cdot\mathbf{v} = 0, \tag{1}$$

$$\frac{d\mathbf{v}}{dt} = \mathbf{g} - \frac{1}{\rho}\nabla p + \nu\nabla^2\mathbf{v} + \frac{1}{\rho}\nabla\cdot\Pi, \tag{2}$$

where $\rho, p, \mathbf{v}$ and $\mathbf{g}$ are fluid density, velocity, pressure and body force, respectively, and $\nu = \eta/\rho$ is the kinematic viscosity. Π is the surface stress given by

$$\Pi = \alpha\frac{1}{|\nabla C|}\left(\frac{1}{d}\mathbf{I}|\nabla C|^2 - \nabla C\nabla C\right), \tag{3}$$

and α is the surface-tension coefficient, d is the spatial dimension and ∇C is the gradient of a color index C which has a unit jump across the interface. Note that the two expressions (constant-density and zero-velocity-divergence) in Eq. (1) are formally equivalent for an incompressible flow.

To discretize Eqs. (1) and (2), two forms of the SPH approximation [6] with a kernel function $W(\mathbf{r})$ can be given as

$$\nabla\psi_i \approx \sigma_i\sum_j\left(\frac{1}{\sigma_i^2} + \frac{1}{\sigma_j^2}\right)\overline{\psi}_{ij}\nabla W_{ij} = \sigma_i\sum_j \mathbf{A}_{ij}\overline{\psi}_{ij}, \tag{4}$$

$$\nabla\psi_i \approx \sigma_i\sum_j\left(\frac{\psi_i}{\sigma_i^2} + \frac{\psi_j}{\sigma_j^2}\right)\nabla W_{ij}, \tag{5}$$

where $\mathbf{A}_{ij} = (\frac{1}{\sigma_i^2} + \frac{1}{\sigma_j^2})\nabla W_{ij}$, $\nabla W_{ij} = \nabla W(\mathbf{r}_i - \mathbf{r}_j)$, and $\mathbf{r}_i - \mathbf{r}_j = \mathbf{r}_{ij} = r_{ij}\mathbf{e}_{ij}$, and $\mathbf{e}_{ij}$ is the normalized vector from particle i to particle j. ψ_i is the value of a smooth variable $\psi(\mathbf{r})$ for a particle and $\overline{\psi}_{ij}$ is an inter-particle averaged value. The particle number density $\sigma_i = \sum_j W_{ij}$ approximates the inverse of the particle volume, hence the particle density is given by

$$\rho_i = m_i\sigma_i \tag{6}$$

where m_i is the mass of particle. In practice, σ_i and m_i are initially chosen for every particle based on the fluid density and particle distribution. Since m_i does not change through out the computation in a mass-conservative incompressible SPH formulation, the constant-density condition requires that σ_i be constant.

2.1. Projection method

Similarly to Ref. [7], a fractional time-step integration approach is used to solve Eqs. (1) and (2). First, a half-time-step velocity is obtained by

$$\mathbf{v}_i^{n+1/2} = \mathbf{v}_i^n + \left(\mathbf{f} - \frac{1}{\rho}\nabla p\right)_i^n\frac{\Delta t}{2}, \tag{7}$$

where $\mathbf{f}$ is the sum of body force, viscous force and surface force. Subsequently, the particle position at the new time-step is calculated by

$$\mathbf{r}_i^{n+1} = \mathbf{r}_i^n + \mathbf{v}_i^{n+1/2}\Delta t, \tag{8}$$

and the particle velocity at the new time-step is obtained by

$$\mathbf{v}_i^{n+1} = \mathbf{v}_i^{n+1/2} + \left(\mathbf{f} - \frac{1}{\rho}\nabla p\right)_i^n\frac{\Delta t}{2}. \tag{9}$$

The two incompressibility conditions in Eq. (1) need to be enforced simultaneously to avoid spurious particle aggregation [7]. The zero-velocity-divergence condition is satisfied by computing the pressure gradients in Eq. (9) to adjust the particle velocity so that a divergence-free velocity field is obtained, whereas the constant-density condition is enforced by correcting the predicted particle position, for details refer to Ref. [7]. In order to cope with the computational issues related to convergence and the reference pressure, we propose in this paper a new approach to enforce the constant-density condition by computing the pressure gradient in Eq. (7) to correct the half-time-step velocity $\mathbf{v}_i^{n+1/2}$ for a constant σ_i, hence constant-density according to Eq. (6). The additional benefit of this approach, as will be shown later, is that large density ratios across the interface can be achieved.

2.1.1. Constant-density condition

We split Eq. (7) into an intermediate step and a correction step. An intermediate velocity $\mathbf{v}_i^{*,n+1/2}$ is obtained by

$$\mathbf{v}_i^{*,n+1/2} = \mathbf{v}_i^n + \frac{\Delta t}{2}\mathbf{f}_i(\mathbf{r}^n, \mathbf{v}^n), \tag{10}$$

and the half-time-step velocity $\mathbf{v}_i^{n+1/2}$ is obtained by

$$\mathbf{v}_i^{n+1/2} = \mathbf{v}_i^{*,n+1/2} - \frac{\Delta t}{2}\left(\frac{\nabla p}{\rho}\right)_i^n. \tag{11}$$

Using Eq. (6), the discretization of the general form of the continuity equation $\frac{d\rho}{dt} = -\rho\nabla\cdot\mathbf{v}$, with the uncorrected intermediate velocity gives

$$\sigma_i^{*,n+1} - \sigma_i^n = -\Delta t\sigma_i^n\nabla\cdot\mathbf{v}_i^{*,n+1/2}. \tag{12}$$

Ideally, Eq. (12) implies that the velocity-divergence-free condition gives zero density variation. However, in practice, as there are already some residual density errors on σ_i^n before the particle moves for another new time step, we actually expect the particle density to evolve back to its initial density σ_i^0. Hence the condition for the half-time-step particle velocity becomes

$$\nabla\cdot\mathbf{v}_i^{n+1/2} = -\frac{\sigma_i^0 - \sigma_i^n}{\Delta t\sigma_i^n}. \tag{13}$$

Taking the divergence of Eq. (11) and substituting Eq. (13) one obtains an equation for the intermediate pressure

$$\nabla\cdot\left(\frac{\nabla p^*}{\rho}\right)_i^n = \Delta t\nabla\cdot\mathbf{v}_i^{*,n+1/2} + \frac{\sigma_i^0 - \sigma_i^n}{\sigma_i^n}. \tag{14}$$

where $p^* = \frac{1}{2}p\Delta t^2$. Note that the divergence of the intermediate velocity on the right-hand side gives the density error introduced by Eq. (10), and the second part gives the accumulated density error before the new time-step. To obtain the discrete form of the velocity-divergence operator, we compute the contribution of the intermediate velocity to the variation of the particle number density by directly taking the time derivative $\frac{d\sigma_i}{dt} = \sum_j \nabla W_{ij}\cdot\mathbf{v}_{ij}$, where $\mathbf{v}_{ij} = \mathbf{v}_i - \mathbf{v}_j$. The discrete form is

$$\sigma_i^{*,n+1} - \sigma_i^n = \Delta t\sum_j \nabla W_{ij}\cdot\mathbf{v}_{ij}^{*,n+1/2}, \tag{15}$$

where $\mathbf{v}_{ij}^{*,n+1/2} = \mathbf{v}_i^{*,n+1/2} - \mathbf{v}_j^{*,n+1/2}$. By comparing Eqs. (15) and (12), the discrete divergence of velocity is

$$\nabla\cdot\mathbf{v}_i^{*,n+1/2} = -\frac{1}{\sigma_i}\sum_j \nabla W_{ij}\cdot\mathbf{v}_{ij}^{*,n+1/2}. \tag{16}$$

2.1.2. Exact projection

If the gradient and the divergence operators are chosen according to the forms of Eqs. (5) and (16), the Poisson operator in Eq. (14) for an exact projection can be discretized as

$$\nabla\cdot\left(\frac{\nabla p^*}{\rho}\right)_i = -\frac{1}{\sigma_i}\sum_j \nabla W_{ij}\cdot\left[\frac{1}{m_i}\sum_k \nabla W_{ik}\left(\frac{p_i^*}{\sigma_i^2} + \frac{p_k^*}{\sigma_k^2}\right) - \frac{1}{m_j}\sum_l \nabla W_{jl}\left(\frac{p_j^*}{\sigma_j^2} + \frac{p_l^*}{\sigma_l^2}\right)\right]. \tag{17}$$

Hence Eq. (14) can be written as

$$\sum_j B_{ij}p_j^* = \sigma_i^n - \sigma_i^0 + \Delta t\sum_j \nabla W_{ij}\cdot\mathbf{v}_{ij}^{*,n+1/2}, \tag{18}$$

where the matrix B_{ij} has the diagonal components

$$B_{ii} = \frac{1}{\sigma_i^2}\sum_j \nabla W_{ij}\cdot\left(\sum_k \frac{\nabla W_{ik}}{m_i} + \frac{\nabla W_{ij}}{m_j}\right), \tag{19}$$

and the off-diagonal components

$$B_{ij} = \frac{1}{\sigma_j^2}\left[\sum_k \nabla W_{ik}\cdot\left(\frac{\nabla W_{ij}}{m_i} - \frac{\nabla W_{kj}}{m_k}\right) - \nabla W_{ij}\cdot\sum_l \frac{\nabla W_{jl}}{m_j}\right]. \tag{20}$$

Note that B_{ij} is only approximately symmetric. Therefore, highly-efficient solvers for non-symmetric linear systems, such as the generalized minimum residual (GMRES (q), q is the number of inner iteration steps without restarting) method, need to be used. With Eqs. (5), (11) and (8), the new particle position can be obtained by

$$\mathbf{r}_i^{n+1} = \mathbf{r}_i^n + \Delta t \mathbf{v}_i^{*,n+1/2} - \frac{1}{m_i}\sum_j \nabla W_{ij}\left(\frac{p_i^*}{\sigma_i^2} + \frac{p_j^*}{\sigma_j^2}\right). \tag{21}$$

2.1.3. Velocity-divergence-free condition

The intermediate velocity at the full-time-step $\mathbf{v}^{*,n+1}$ is obtained by

$$\mathbf{v}_i^{*,n+1} = \mathbf{v}_i^{*,n+1/2} + \mathbf{f}_i(\mathbf{r}^n, \mathbf{v}^n)\frac{\Delta t}{2}. \tag{22}$$

The velocity at the full-time-step $\mathbf{v}^{n+1}$ is obtained by

$$\mathbf{v}_i^{n+1} = \mathbf{v}_i^{*,n+1} - \left(\frac{\nabla p'}{\rho}\right)_i^n, \tag{23}$$

where $p' = \frac{1}{2}p\Delta t$. To enforce the velocity-divergence-free condition at the new time-step, the divergence of Eq. (23) is taken, and by $\nabla_i \cdot \mathbf{v}^{n+1} = 0$ one obtains the required pressure distribution from

$$\nabla \cdot \left(\frac{\nabla p'}{\rho}\right)_i^n = \nabla_i \cdot \mathbf{v}^{*,n+1}. \tag{24}$$

According to Ref. [7], Eq. (24) is discretized as

$$\sum_j \frac{A_{ij}}{r_{ij}}\frac{p'_{ij}}{\rho_i + \rho_j} = \frac{1}{2}\sum_j A_{ij}\left(\frac{\eta_i \mathbf{v}_i^{*,n+1} + \eta_j \mathbf{v}_j^{*,n+1}}{\eta_i + \eta_j}\right)\cdot \mathbf{e}_{ij}, \tag{25}$$

where $A_{ij} = \mathbf{A}_{ij}\cdot\mathbf{e}_{ij}$, $p'_{ij} = p'_i - p'_j$, and η_i and η_j are viscosities for the two particles. The pressure gradient in Eq. (23) is discretized as

$$\left(\frac{\nabla p'}{\rho}\right)_i = \frac{1}{m_i}\sum_j A_{ij}\frac{\rho_i p'_j + \rho_j p'_i}{\rho_i + \rho_j}\mathbf{e}_{ij}. \tag{26}$$

Note that the zero-velocity-divergence constraint is enforced by an approximate projection because the divergence of the uncorrected full-time-step velocity field is discretized in a conservative form based on Eq. (4), which is very different from that of Eq. (18).

2.2. Implementation

The overall procedure of the current projection method can be summarized as follows:

(1) Calculate the intermediate half-time-step velocity by Eq. (10).
(2) Obtain the intermediate pressure for particle density correction by solving Eq. (18).
(3) Update the new time-step particle position by Eq. (21).
(4) Calculate the intermediate full-time-step velocity by Eq. (22).
(5) Obtain the intermediate pressure for full-time-step velocity correction by solving Eq. (25).
(6) Update the new time-step particle velocity by Eq. (23).

In practice, the convergence criterion for Step 2 is chosen such that the mean or maximum predicted density error, estimated by the average residual or maximum residual of Eq. (18), is less than a certain threshold, usually 0.1%. Numerical experiments suggest that no extra reference pressure is need to be superimposed when updating the new time-step particle position by Step 3. When updating the new time-step velocity, Step 6, for the zero-velocity-divergence constraint, the reference pressure is simply set as the magnitude of the minimum negative pressure obtained from the solution of the Poisson equation, which is different from the prescribed reference pressure in [7].

2.3. Time-step criteria

The same time-step criteria as in [7] for stable time integration, including a CFL condition, a viscous-diffusion condition and surface-tension condition must be satisfied. In [7] there is a time-step criterion based on the prescribed reference pressure, which is proportional to the maximum density. This time-step criterion can lead to extremely small time-steps for problems with large density ratios. In this work, this difficulty can be alleviated because, according to the proposed treatment for the reference pressure, the tensile instability is less pronounced and a time-step criterion based on the reference pressure is not necessary. However, as the conservative discretization of the pressure gradient in an SPH method produces residual fluctuations proportional to the pressure magnitude, very large pressure values may still cause a stability problem. From Eq. (14), it can be seen that the difference of the pressure gradient is approximately proportional to the magnitude of

the right-hand side, which can result in large pressure gradients and eventually lead to large pressure values. Therefore, the following bounds are enforced

$$|\Delta t \nabla \cdot \mathbf{v}_i^{*,n+1/2}|_{\max} \leqslant \epsilon_1 \quad \text{and} \quad \left|\frac{\sigma_i^0 - \sigma_i^n}{\sigma_i^n}\right|_{\max} \leqslant \epsilon_0. \tag{27}$$

Note that, since Eq. (27) is not directly related to the reference pressure or the density ratio, the related obstacle of small time-step sizes is alleviated. Typically, one can choose $\epsilon_0 = 0.01$ and $\epsilon_1 = 0.1$ which need to be satisfied by the iterative scheme. The relation $\epsilon_1 \gg \epsilon_0$ is found through numerical experimentation, which indicates that the introduced density error due to the uncorrected velocity (i.e. the first relation in (27)) is much larger than the accumulated density error (i.e. the second relation in (27)). The first relation gives a new global time-step criterion

$$\Delta t \leqslant \epsilon_1 |\nabla \cdot \mathbf{v}^{*,n+1/2}|_{\max}^{-1}. \tag{28}$$

If the second relation is not satisfied the accumulated density error is large, and a further correction on particle position and velocity is enforced before a new time-step. This is done by the same projection procedures as above but with zero time-step size.

3. Numerical examples

The following two-dimensional numerical examples serve to validate the proposed incompressible multi-phase SPH method. For all cases a quintic spline kernel [10] is used as smoothing function. A constant smoothing length, which is kept equal to the initial distance between the neighboring particles, is used for all test cases. The discretizations of viscous force and surface force follow Ref. [6]. As elliptic solver a diagonally preconditioned GMRES (q) method is used. If not mentioned otherwise, no-slip wall boundary conditions are implemented following the approach of Cummins and Rudman [2].

3.1. Two-dimensional Taylor–Green flow

The two-dimensional viscous Taylor–Green flow is a periodic array of vortices, where the velocity

$$\begin{aligned} u(x,y,t) &= -Ue^{bt}\cos(2\pi x)\sin(2\pi y) \\ v(x,y,t) &= Ue^{bt}\sin(2\pi x)\cos(2\pi y) \end{aligned} \tag{29}$$

is an exact solution of the incompressible Navier–Stokes equation. $b = -\frac{8\pi^2}{\mathrm{Re}}$ is the decay rate of velocity field. We consider a case with $Re = 100$, which has been used to test different incompressible SPH methods [1,4,7]. The computational set-up is the same as that of [7]. The computation is performed on a domain $0 < x < 1$ and $0 < y < 1$ with periodic boundary conditions in both directions. The initial particle velocity is assigned according to Eq. (29) by setting $t = 0$ and $U = 1$. Same as in [7], the initial particle configuration is taken from previously stored particle positions (relaxed configuration). In order to study the convergence properties the calculation is carried out with 450, 900, 3600 particles, respectively.

Fig. 1 shows the calculated positions of particles and vorticity profiles, respectively, at $t = 1$ with 3600 particles. It can be observed that a uniform particle distribution without clustering is produced. The current SPH simulation recovers the theoretical solution quite well with somewhat larger errors in regions close to the centers of vortex cells. Fig. 2(a) shows the calculated decay of the maximum velocity of the flow with different resolutions.

It can be observed that for low resolution results, the predicted Reynolds number is slightly smaller than the theoretical value. However, the predicted Reynolds number converges to the theoretical value with increasing resolution. Note that, with only 450 particles, the accuracy of the current simulation is comparable with that of [4] with 3600 particles (see their Fig. 8), in which only the constant-density constraint is implemented by a non-linear iterative approach. We measure the overall accuracy by L_1 errors

$$L_1 = \frac{\sum_{i=1}^{N}\left|U^{ex} - U^{\mathrm{SPH}}\right|}{\sum_{i=1}^{N}\left|U^{ex}\right|}, \tag{30}$$

where U^{SPH} and U^{ex} are the simulated and theoretical velocities, respectively, N is the number of particles. The L_1 errors with different resolutions are shown in Fig. 2(b), which indicate an super-linear convergence rate.

While in the present method the reference pressure is used only for the zero-velocity-divergence constraint as described in the last paragraph of Section 2.2, it is prescribed as a constant value in [7]. Although the magnitude of the reference pressure can be determined by considering the force balance in the equation of motion, the optimal value which gives stable and accurate results usually is obtained empirically. For example, for the current case with 900 particles, the direct implementation with the reference pressure value 1 gives unacceptable errors increasing with time, as shown in Fig. 2 for the lines denoted as A. From the decay of the maximum velocity, one can find that the flow is over-dissipative which suggests that a large numerical viscosity is introduced by the reference pressure. By numerical experimentation, more suitable values are found 2 for the constant-density constraint and 0.02 for the zero-velocity-divergence constraint, by which the numerical error decreases considerably, as shown in Fig. 2(b) for the line denoted as B. Note that a seemingly higher accuracy than that

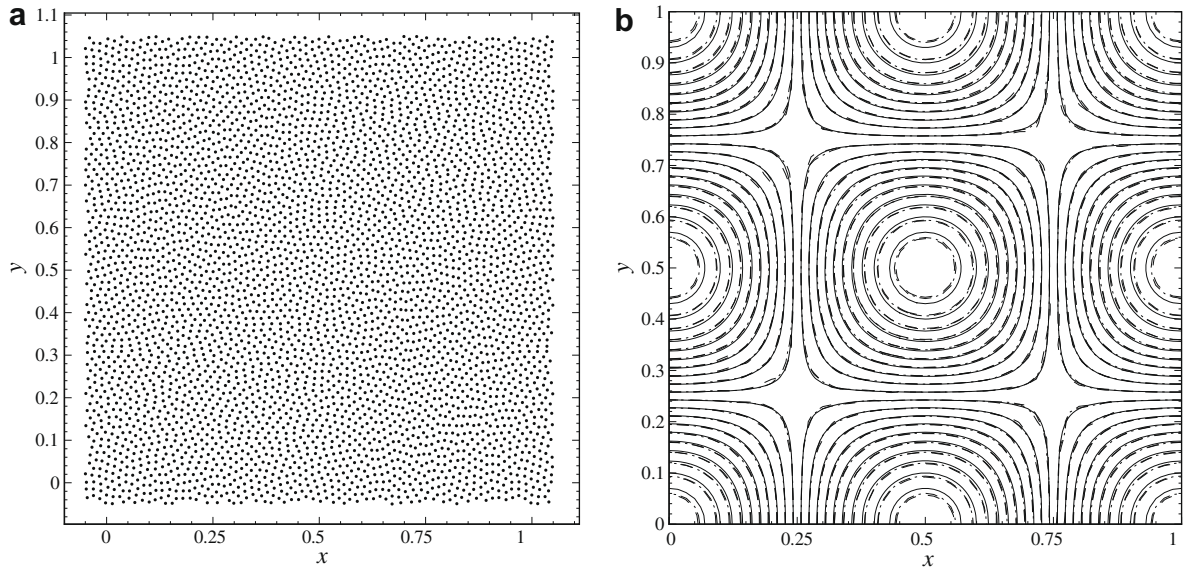

Fig. 1. Taylor–Green problem at $t = 1$ with 3600 particles: (a) positions of particles, (b) simulated vorticity profile (dashed line: results of [7] with the optimal reference pressure, dash-dot line: current) and analytical solution (solid line).

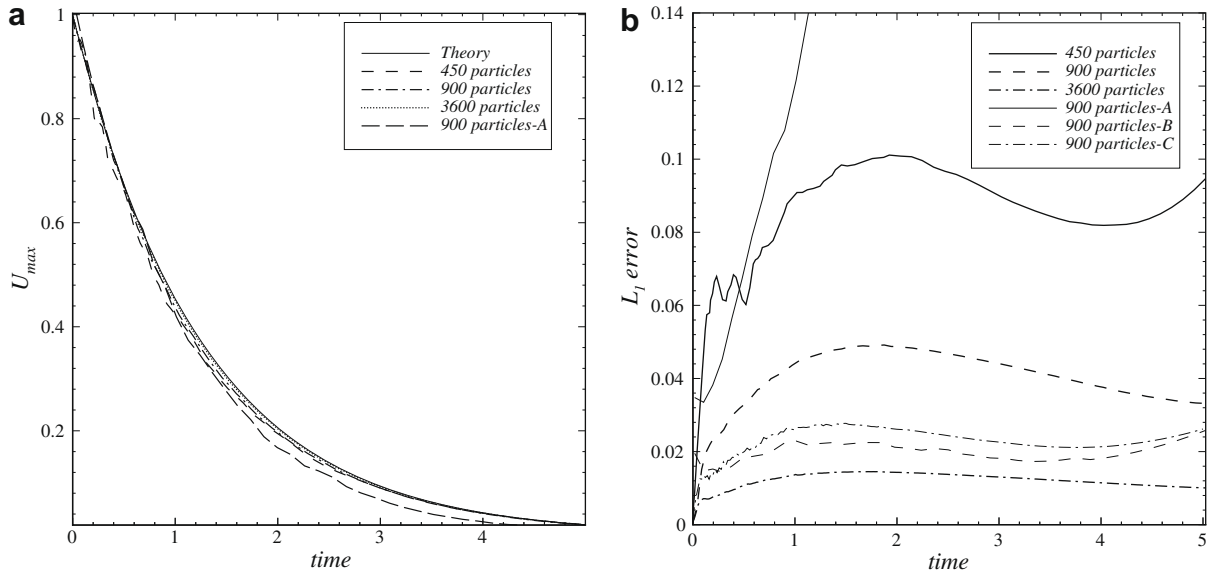

Fig. 2. Taylor–Green problem with different resolutions and reference pressure options: (a) decay of the maximum velocities, (b) history of L_1 errors. (A) The method in Ref. [7] with a directly applied reference pressure, (B) the method in Ref. [7] with an optimal reference pressure, and (C) the present method with smaller time-step sizes.

of the present method is due to the fact that in Ref. [7] the time-step size is about half of the current as result of the time-step restriction due to the reference pressure. With approximately the same time-step sizes, comparable accuracy can also be achieved by the present method, as shown in Fig. 2(b) for the line denoted as C. Furthermore, for even higher resolution, there is no notable difference between the present results and those in Ref. [7] obtained with optimal reference pressure, as shown in Fig. 1(b).

3.2. Capillary wave

We consider two problems of liquid drop oscillation under the action of capillary forces. The first problem, taken from Refs. [9,6,7], is a liquid drop oscillating in another phase with the same density and viscosity. In the second problem, the oscillation is tested by changing the density and viscosity ratios between the liquid drop and the surrounding fluid.

For the first problem, the computational setup is the same as that of [6] and [7]. The computation is performed on a domain $0 < x < 1$ and $0 < y < 1$ using fluids of the same density $\rho_d = \rho_c = 1$ and equal viscosity $\eta_d = \eta_c = 0.05$. A droplet of radius $R = 0.1875$ is placed at the domain center and the surface-tension coefficient is $\alpha = 1$. To all particles a divergence-free initial velocity $v_x = V_0 \frac{x}{r_0}(1 - \frac{y^2}{r_0 r}) \exp(-\frac{r}{r_0})$ and $v_y = V_0 \frac{y}{r_0}(1 - \frac{x^2}{r_0 r}) \exp(-\frac{r}{r_0})$ is assigned, where $V_0 = 10, r_0 = 0.05$, and r is the distance from the position (x, y) to the droplet center. In order to study the convergence properties the calculation is carried out with 900, 3600, 14400 particles, respectively.

Fig. 3 shows the positions of the droplet particles at 4 selected time instants with 14400 particles. It is observed that particle distribution is in quite good agreement with the results of Refs. [6] and [7] (their Fig. 4s). Fig. 4 gives the variation of the center-of-mass position and kinetic energy of the upper right 1/4 part of the droplet with different resolutions. Super-linear convergence rates are obtained for both mass center position and kinetic energy by calculating the relative error between different resolutions. Note that, compared to the results in Ref. [7] (their Fig. 5), again the present low resolution results is less accurate because of a larger time-step. With increasing resolution these differences become less significant. The present computed first period at the highest resolution is about 0.344 which is very close to the result of 0.35 in [7].

For the second problem, the initial configuration is the same as that of the first problem. The calculations are carried out with 3600 particles.

The density and viscosity of the liquid drop are set to $\rho_d = 1$ and $\eta_d = 10^{-1}$, respectively. Several cases with different density ratios, $\gamma = \rho_d/\rho_c$, up to 1000, and viscosity ratios, $\lambda = \eta_d/\eta_c$, up to 100, between the liquid drop and the surrounding

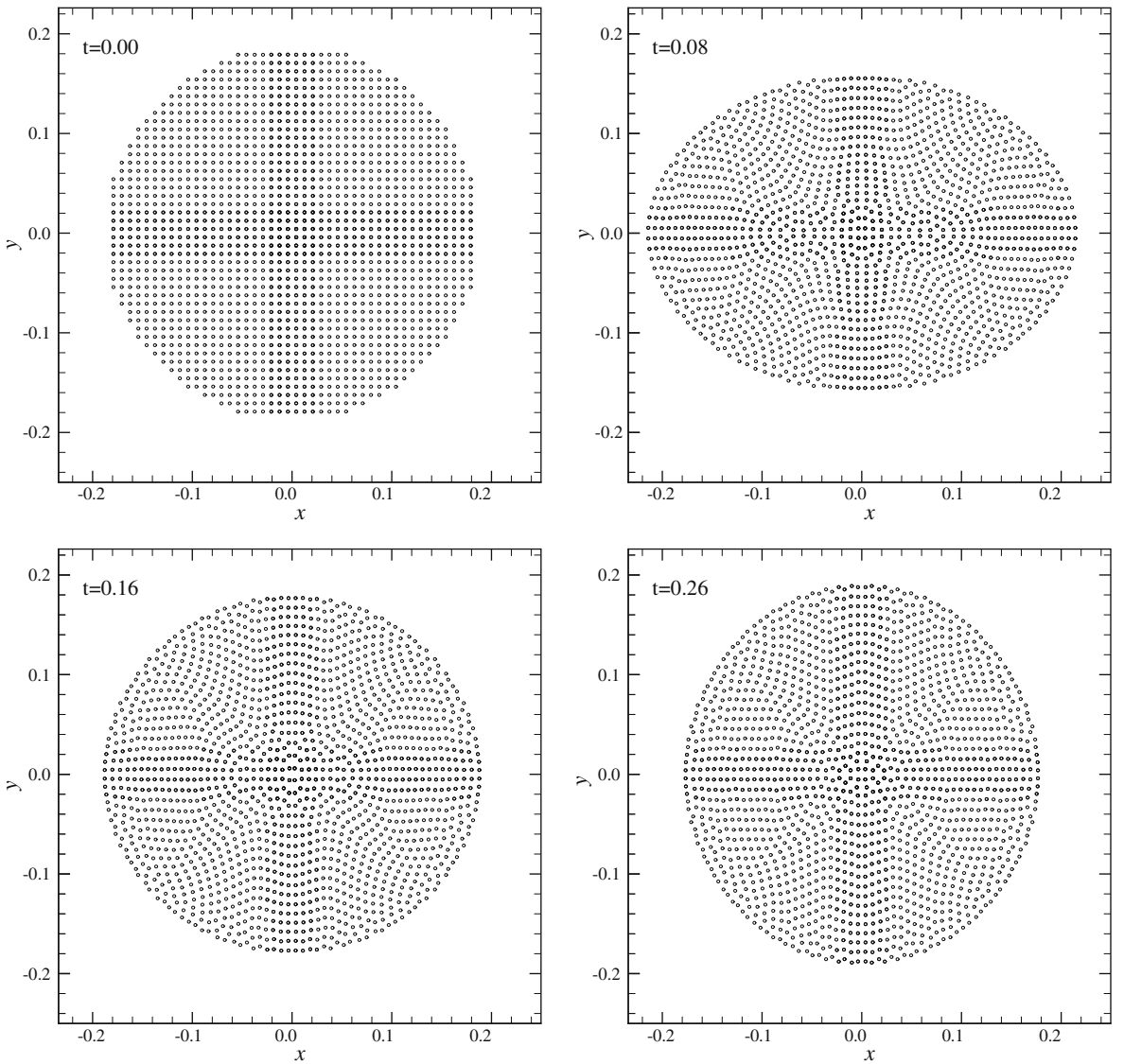

Fig. 3. Droplet oscillation with $\rho_d/\rho_l = 1$: particle positions at $t = 0, t = 0.08, t = 0.16$ and $t = 0.26$.

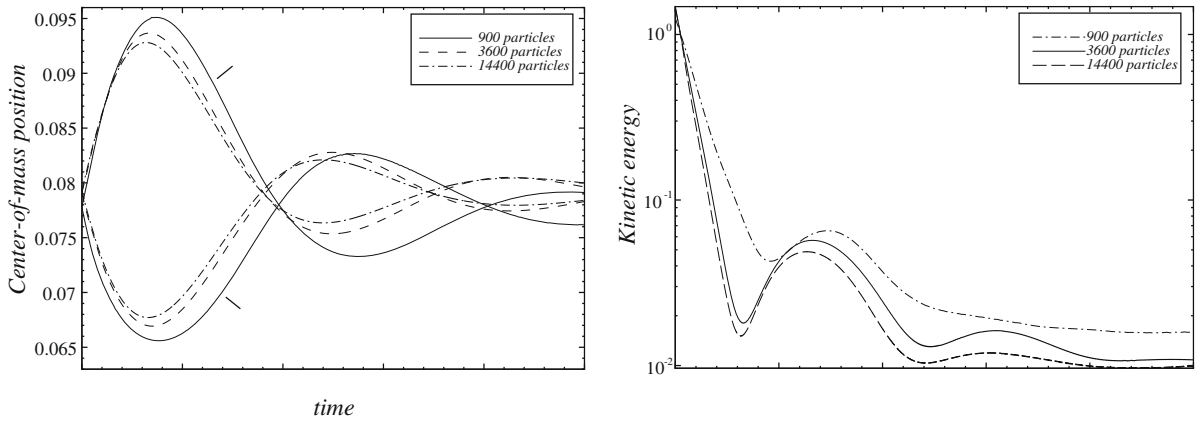

phase are calculated. Note that, for this problem the method in [7] similarly as other projection SPH faces serious difficulty on constant-density constraint. When the density ratio is high, i.e. $\gamma = 100$ and $\gamma = 1000$, the iteration fails to converge to the permitted maximum density error, that is, 1%. Further studies suggested that this problem is caused by the large reference pressure due to the high density ratio. A large reference pressure can produce large density perturbations, comparable to the permitted maximum density error, and prevents convergence.

Fig. 5 gives the variation of the center-of-mass position and velocity of the upper right 1/4 part of the droplet. One can find that when $\gamma = 1$ and $\lambda = 1$, as the viscosity is larger than that of the first problem, the oscillation decays faster and the first period increases slightly. When the ambient phase becomes more viscous, $\lambda = 0.1$, the capillary wave is damped very fast and there is essentially no oscillation. If one keeps the viscosity ratio $\lambda = 1$ and decreases the ambient phase density as $\gamma = 10$, the oscillation decay is comparable with the case with $\lambda = 1$ and $\gamma = 1$, but the first period is shortened considerably. When both the density ratio and viscosity ratio increase, the oscillation decay becomes slower and the first period becomes shorter. When the density ratio is $\gamma = 1000$ and the viscosity ratio $\lambda = 100$, which corresponds approximately to a water–air pairing, the oscillation decay and oscillation period approach a limit which depends on the density and viscosity of the liquid drop only. The measured first period is about 0.205 which recovers the theoretical period $\tau = 2\pi\sqrt{\frac{R^3\rho_l}{6\alpha}} \approx 0.208$ of a free-drop oscillation quite well.

3.3. Rayleigh–Taylor instability

We consider two Rayleigh–Taylor instability problems. The first problem which has been studied in Refs. [2] and [7] is the instability of two continuous phases under the action of gravity. The second problem is the instability of a continuous phase and a bubbly phase.

For the first problem, the computation is performed on a domain $0 < x < 1$ and $0 < y < 2$. Initially, the particles are placed on regular lattice positions. In the lower part of the domain are particles with density $\rho_l = 1.0$. In the upper domain, defined

by $y > 1 - 0.15\sin(2\pi x)$, are particles with density $\rho_u = 1.8$. The Reynolds number is set to $Re = 420$ and the Froude number is set to $Fr = 1$. No surface-tension is included. The initial particle velocity is set to zero. The calculation is carried out with 7200 particles. The computational setup is the same as that of Ref. [7].

The calculated particle positions at times $t = 1, t = 3$ and $t = 5$ are shown in Fig. 6. The general features show a good agreement with the results in Ref. [7] (see their Fig. 10), which produces more interfacial vorticity than [2] because of the sharp-interface representation. However, the present results show even stronger deposition of vorticity at late times, when the secondary plumes, which usually can only be found in high resolution computations, emerge from the initial plumes. This indicates that the present method introduces significantly less numerical viscosity than previous incompressible SPH [2,7]. The results obtained in Ref. [7] suggests that the reference pressure is over-estimated. However, since sufficiently large reference pressure is always needed for numerical stability, smaller reference pressure may reduce numerical viscosity but can cause a stability problem. This stability problem leads the particles of the top layer moving gradually down from the wall and producing a void region (not shown here).

For the second problem, the computational setup is similar, but the average density $\rho_l = 1.0$ of the lower part of the domain is achieved approximately by randomly distributing the same particles as in the upper part of the domain and other particles with 1/100 density and 1/10 viscosity, respectively. Therefore, the lower part of the domain is a bubbly region. The calculation is carried out with 12,800 particles, in which several hundreds bubbles are embedded in the continuous fluid, as shown if Fig. 7(a). This problem is very challenging for conventional multi-phase methods, by which either the individual bubbles cannot be accurately resolved because of the strongly smeared interface, as e.g. for front-capturing methods, or the mass of the bubbles can not be preserved, as e.g. for front-tracking methods. The practical applicability of these methods is currently limited to the study of problems involving only a small number of bubbles, typically $O(100)$ or less [5,8]. In the present method, the bubbles are fully resolved because of the sharp-interface model and the mass of the bubbles is constant because of the fully conservative scheme. It should be stressed that this problem is chosen to show the robustness of the present method. However, we are not aware of a reference experiment or numerical solution available in the literature for comparison.

The calculated positions of particles at times $t = 3$ and $t = 4.5$ are shown in Fig. 7(b) and (c). Although we can not find numerical or experimental work which can be compared directly to the present simulation, it is apparent that the instability evolution resembles that of the first problem. However, the interfaces between the continuous phase and the bubbly phase, and the bubbly phase itself are not smooth, and the interfacial disturbances can develop a more complex behavior. Multiple "bubbles" and "spikes" are formed, by which a very complicated flow field develops much earlier than for the first problem (see Fig. 7(b)). Another major difference is that the main spike moves faster. As shown in Fig. 7(c), the main spike reaches the

4. Concluding remarks

We have developed a new method for enforcing the constant-density constraint for the incompressible multi-phase SPH method. A new exact projection formulation is proposed by which the reference pressure issue is handled in a straightforward way. In addition, without the previous time-step restriction related to the reference pressure, the present method allows for computations of flows with large density ratios. Numerical examples are investigated and compared with analytic solutions and previous results. The results show that the method can be applied to incompressible single-phase and multi-phase flows with a wide range of density and viscosity ratios.

References

[1] A.K. Chaniotis, D. Poulikakos, P. Koumoutsakos, Remeshed smoothed particle hydrodynamics for the simulation of viscous and heat conducting flows, J. Comput. Phys. 182 (2002) 67.
[2] S.J. Cummins, M. Rudman, An SPH projection method, J. Comput. Phys. 152 (1999) 584.
[3] C.T. Dyka, R.P. Ingel, An approach for tension instability in smoothed particle hydrodynamics (SPH), Comput. Struct. 57 (4) (1995) 573–580.
[4] M. Ellero, M. Serrano, P. Espanol, Incompressible smoothed particle hydrodynamics, J. Phys. Comput. 226 (2007) 1371.
[5] A. Esmaeeli, G. Tryggvason, A direct numerical simulation study of the buoyant rise of bubbles at $O(100)$ Reynolds number, Phys. Fluids 17 (2005) 093303.
[6] X.Y. Hu, N.A. Adams, A multi-phase SPH method for macroscopic and mesoscopic flows, J. Comput. Phys. 213 (2006) 844.
[7] X.Y. Hu, N.A. Adams, An incompressible multi-phase SPH method, J. Comput. Phys. 227 (2007) 264–278.
[8] J. Lu, S. Biswas, G. Tryggvason, A DNS study of laminar bubbly flows in a vertical channel, Int. J. Multiphase Flow 32 (6) (2006) 643–660.
[9] J.P. Morris, Simulating surface tension with smoothed particle hydrodynamics, Int. J. Numer. Meth. Fluids 33 (1999) 333.
[10] J.P. Morris, P.J. Fox, Y. Zhu, Modeling low Reynolds number incompressible flows using SPH, J. Comput. Phys. 136 (1997) 214.
[11] J. Pozorski, A. Wawreńczuk, Sph computation of incompressible viscous flows, J. Theor. Appl. Mech. 40 (2002) 917.
[12] S. Shao, E.Y.M. Lo, Incompressible SPH method for simulating Newtonian and non-Newtonian flows with a free surface, Adv. Water Resour. 26 (2003) 787.
[13] J.W. Swegle, D.L. Hicks, S.W. Attaway, Smoothed particle hydrodynamics stability analysis, J. Comput. Phys. 116 (1) (1995) 123–134.